Journal of Sol-Gel Science and Technology (2023) 107:810–820
https://doi.org/10.1007/s10971-023-06170-2

ORIGINAL PAPER: SOL-GEL, HYBRIDS AND SOLUTION CHEMISTRIES

A comparative study of structural, magnetic, and thermal properties of $Cu_xFe_{3-x}O_4$ nanoparticles prepared in open and closed systems using solution combustion synthesis

Sümran Bilgin[1] · **Ümit Alver**[1]

Received: 15 March 2023 / Accepted: 12 June 2023 / Published online: 23 June 2023

Abstract

The $Cu_xFe_{3-x}O_4$ nanoparticles with a cubic structure and varying ratios of copper (Cu) and iron (Fe) ($x = 0.75, 1, 1.25$) were synthesized using the one-step solution combustion synthesis (SCS) method. $Cu_xFe_{3-x}O_4$ nanoparticles were synthesized via solution combustion synthesis, utilizing copper nitrate and iron nitrate as the oxidizing agents, and glycine as the fuel. The synthesis was carried out under different conditions, including the presence and absence of air, to investigate their effects on the final product. X-ray diffraction (XRD), the Fourier transform infrared spectroscopy (FTIR), thermal gravimetric analysis (TGA) and differential scanning calorimetry analysis (DSC), scanning electron microscopy (SEM), transmission electron microscopy (TEM), high-resolution (HR) TEM and vibrating sample magnetometer (VSM) measurements were used to confirm the formation and structure of the as-prepared nanopowders. The use of the open system during the synthesis process leads to a higher occurrence of secondary phase formation in the structure of the material. The findings obtained from various analysis confirms that the closed system used in the study yields efficient results.

Graphical Abstract

$Cu_xFe_{3-x}O_4$ nanoparticles were synthesized via solution combustion synthesis in a closed system.

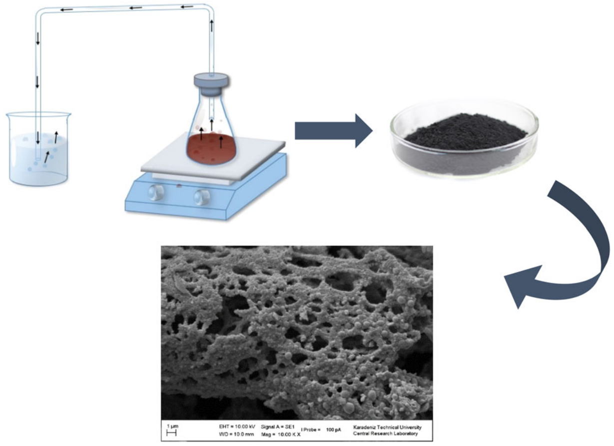

Keywords $Cu_xFe_{3-x}O_4$ · Solution combustion synthesis · Magnetic properties · Thermal properties

---

✉ Sümran Bilgin
sumranbilgin@ktu.edu.tr

[1] Faculty of Engineering, Department of Metallurgical and Materials Engineering, Karadeniz Technical University, 61080 Trabzon, Turkey

Highlights

- $Cu_xFe_{3-x}O_4$ nanoparticles were synthesized using the solution combustion synthesis.
- Effect of open and closed systems were investigated on nanoparticle properties.
- Structural, magnetic, and thermal properties were studied in detail.
- The advantages of a closed system were demonstrated.

1 Introduction

Nanoscale ferrite particles have attracted so much attention due to their size-dependent properties, surface reactivity, and surface effect (large surface-to-volume ratio). Generally, ferrites are of MFe_2O_4 cubic-spinel structured materials and by adjusting and replacing different M^{2+} cations in this structural formula, which are especially transition metals, it can be created a wide range of superior optical, electrical, and magnetic properties. Various nanoscale ferrites such as $NiFe_2O_4$ [1], $CoFe_2O_4$ [2], $ZnFe_2O_4$ [3], $CuFe_2O_4$ [4], and $MnFe_2O_4$ [5] have been successfully synthesized for different applications such as magnetic materials, supercapacitors, semiconductors, microwave absorbents, etc. Among these cubic spinel-structured materials, copper iron oxides ($CuFe_2O_4$) are of great interest due to their low cost, ease of preparation, good chemical stability, and interesting physical properties [6]. Copper ferrites exhibit an inverse spinel structure. The inverse spinel structure contains both octahedral and tetrahedral cation sites. The Fe^{3+} cations occupy tetrahedral (A) and octahedral (B) sites [7–9]. The Cu^{2+} cations are coordinated only in the octahedral sites and this causes reduced lattice symmetry from cubic to tetragonal, which is called the Jahn–Teller effect [7, 10]. $CuFe_2O_4$ is cubic at elevated temperatures (>360 °C) and tetragonal at room temperature.

$CuFe_2O_4$ has been used as a candidate for many applications such as gas sensors [11], Li-ion storage [12], magnetic devices [13], and catalysts [8]. Spinel $CuFe_2O_4$ has been synthesized in several ways including hydrothermal [14], sol-gel [15], solvothermal [16], chemical spray pyrolysis [17], chemical co-precipitation [18], and solution combustion method [19]. Among these, conventional solution combustion synthesis (SCS) has emerged as an extensively employed technique to fabricate nanomaterials, especially for narrow stoichiometric ranges, due to its advantages of short preparation time, low energy consumption, and being environmentally friendly [20]. Solution combustion synthesis is a single-step, low-cost, and rapid process which involves a self-sustained and exothermic reaction between an oxidizer (typically, metal salts such as nitrates, sulfates, and carbonates) and a fuel (reducing agents such as urea, glycine, citric acid, etc.). Characteristics of the SCS process are governed by the oxidizer, typically an aqueous solution of cation precursors, the fuel source, and the utilization of heat. Among the different salts, metal nitrates are widely used for solution combustion synthesis owing to their water solubility and efficient oxidizing of NO^{3-} groups [21]. The important parameters that influence the properties of nanoparticles obtained by solution combustion synthesis are the type of fuel, fuel-to-oxidizer ratio, the use of excess oxidizer, ignition temperature, etc [22]. Among the various control parameters in a combustion process, fuels play an important role in determining the morphology, phase, and particulate properties of the final product. Fuels are generally organic compounds that contain carboxylic acid or amine functional groups. These fuels serve two main purposes: form CO_2 and H_2O and liberate heat during the combustion, form complexes with metal ions for homogeneous solution [23]. The large number of gaseous products released during the solution combustion process prevents agglomeration and ensures a large number of pores and a high surface area. Among the fuels which are utilized in combustion synthesis, glycine is considered to be an ideal fuel. Glycine is an amino acid that contains a carboxylic acid group at one end and an amino group at the other end, so glycine prevents selective precipitation of cations in solution [24]. The complex formation supports a homogeneous mixture and provides to obtain multi-component oxides by preventing the cations segregation. The local temperature increases up to 1000–2000 °C during the combustion process and helps to prevent the formation of metal oxides, which require calcination at high temperatures after synthesis [25].

In the present work, solution combustion synthesis was utilized to obtain nanocrystalline ferrites with the general formula of $Cu_xFe_{3-x}O_4$. In order to understand the effect of copper (Cu) and iron (Fe) different ratios were used ($x = 0.75$, 1, 1.25). Synthesis processes were carried out in an open system and a closed system to demonstrate the effect of the presence of air. Solution combustion synthesis of $Cu_xFe_{3-x}O_4$ nanoparticles was conducted using glycine as fuel. It was observed that the closed system led to a well-crystalline structure.

2 Experimental procedure

Nanocrystalline copper ferrites $Cu_xFe_{3-x}O_4$ ($x = 0.75$, 1, 1.25) were obtained by the solution combustion method. Analytical grade copper nitrate trihydrate ($Cu(NO_3)_2{\cdot}3H_2O$) and iron nitrate nonahydrate ($Fe(NO_3)_3{\cdot}9H_2O$) were used as oxidizers and glycine ($C_2H_5NO_2$) was used as fuel. Syntheses were performed in different ratios and different air conditions to investigate the effect of air. The synthesis of S1, S3, and S5 nanoparticles was carried out in the presence of air, i.e., in an open system. The synthesis of S2, S4, and S6 nanoparticles, on the other hand, was carried out in a closed system without the presence of air. The ratios represent copper nitrate trihydrate, iron nitrate nonahydrate, and glycine, respectively (Table 1):

Sample 1 (S1). Open system, in a beaker (250 ml), in a ratio of 0.75: 2.25: 4.4 (18.12 g: 90.9 g: 33 g; $Cu(NO_3)_2{\cdot}3H_2O$: $Fe(NO_3)_3{\cdot}9H_2O$: $C_2H_5NO_2$), (Fig. 1a).

Sample 2 (S2). Closed system, in Erlenmeyer flask (500 ml) having a rubber plug and a glass pipe with an outlet to remove gases that released during the combustion, in a ratio of 0.75: 2.25: 4.4 ($Cu(NO_3)_2{\cdot}3H_2O$: $Fe(NO_3)_3{\cdot}9H_2O$: $C_2H_5NO_2$), (Fig. 1b).

Sample 3 (S3). Open system, in a beaker, in a ratio of 1: 2: 4.4 (24.16 g: 80.80 g: 33 g; $Cu(NO_3)_2{\cdot}3H_2O$: $Fe(NO_3)_3{\cdot}9H_2O$: $C_2H_5NO_2$).

Sample 4 (S4). Closed system, in Erlenmeyer flask having a rubber plug and a glass pipe with an outlet to remove gases that released during the combustion, in a ratio of 1: 2: 4.4 ($Cu(NO_3)_2{\cdot}3H_2O$: $Fe(NO_3)_3{\cdot}9H_2O$: $C_2H_5NO_2$).

Sample 5 (S5). Open system, in a beaker, in a ratio of 1.25: 1.75: 4.4 (30.2 g: 70.70 g: 33 g; $Cu(NO_3)_2{\cdot}3H_2O$: $Fe(NO_3)_3{\cdot}9H_2O$: $C_2H_5NO_2$).

Sample 6 (S6). Closed system, in Erlenmeyer flask having a rubber plug and a glass pipe with an outlet to remove gases that released during the combustion, in a ratio of 1.25: 1.75: 4.4 ($Cu(NO_3)_2{\cdot}3H_2O$: $Fe(NO_3)_3{\cdot}9H_2O$: $C_2H_5NO_2$).

Table 1 The molar ratios for open and closed systems

Sample	System	Ratio ($Cu(NO_3)_2{\cdot}3H_2O$: $Fe(NO_3)_3{\cdot}9H_2O$: $C_2H_5NO_2$)
S1	Open system	0.75: 2.25: 4.4
S2	Closed system	0.75: 2.25: 4.4
S3	Open system	1: 2: 4.4
S4	Closed system	1: 2: 4.4
S5	Open system	1.25: 1.75: 4.4
S6	Closed system	1.25: 1.75: 4.4

The proper amounts of starting raw materials were dissolved in distilled water and completely mixed to obtain a clear solution. The resulting solutions were rapidly heated to 300 °C on a hot plate to trigger the combustion reaction. By increasing temperature, the solution started to evaporate thereby, the gel formed and in the final stage, the gel was ignited by letting out a large number of gases. Afterward, a self-sustained exothermic reaction occurred and the solution began to smoldering. The same reactions occurred for each sample. As a result of the combustion, black and voluminous nanoparticles were obtained.

The prepared $Cu_xFe_{3-x}O_4$ nanoparticles were analyzed by X-ray diffractometer (XRD, Philips X'Pert Pro, $\lambda = 0.154056$ nm) using Cu-Kα radiation. The Fourier Transform Infrared Spectroscopy (Shimadzu IRSpirit model) device was used to determine the molecular structure of the powders. Thermal gravimetric analysis (TGA) and differential scanning calorimetry analysis (DSC) of the precursors were characterized using the Linseis brand PT1600 DSC/DTA/TG device. Thermal analyses were performed from 20 to 1200 °C with a heating rate of 20 °C/min. The morphology of the nanoparticles was observed using scanning electron microscopy (Zeiss EVO LS10). The particle size was analyzed through a and transmission electron microscopy (TEM) using FEI Talos F200S microscope operating at an accelerating voltage of 200 kV in high-resolution (HR) mode. The magnetization measurements were carried out using a vibrating sample magnetometer (Quantum Design SQUID) at room temperature.

3 Results and discussion

3.1 Structural analysis

The solution combustion synthesis is a redox reaction and causes explosions if not controlled well. The combustion of copper nitrate, iron nitrate, and glycine undergoes a self-propagating and non-explosive reaction.

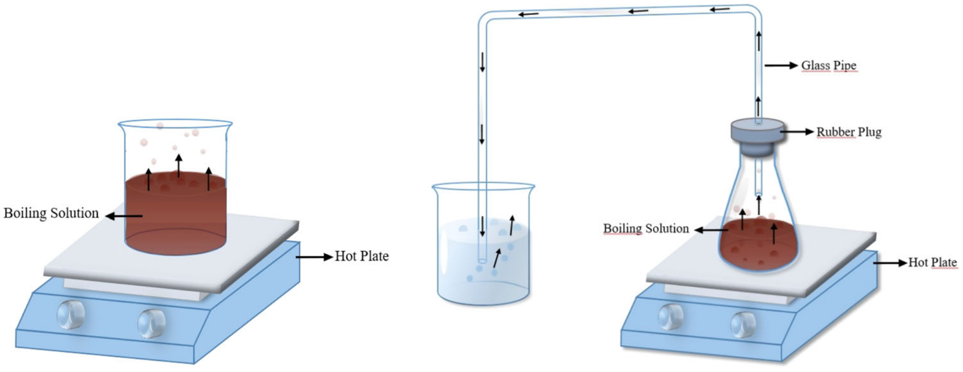

a) b)

Fig. 1 Schematic illustration of solution combustion synthesis for (**a**) open system and (**b**) closed system

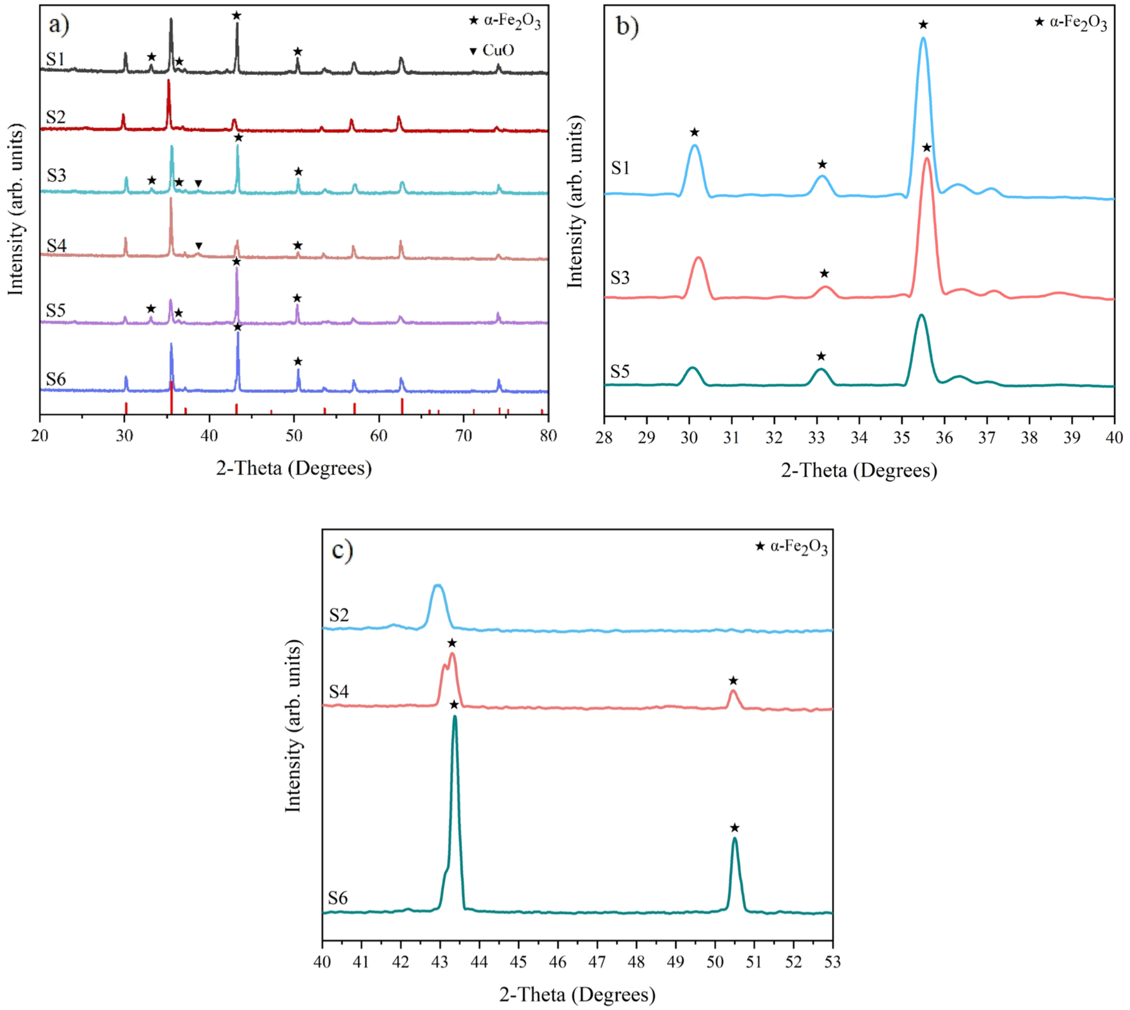

Fig. 2 **a** XRD patterns of $Cu_xFe_{3-x}O_4$ (x = 0.75, 1, 1.25) nanoparticles synthesized by solution combustion synthesis at different conditions. Comparison of peak intensities and peak positions for (**b**) S1, S3, and S5, (**c**) S2, S4, and S6

In the solution combustion process, the molar ratio is a significant factor affecting the combustion behavior, morphology, and specific surface area of the products. On the basis of propellant chemistry, combustion reactions for different ratios can be represented as follows:

$$\begin{aligned}&0.75\,Cu(NO_3)_2{\cdot}3H_2O + 2.25\,Fe(NO_3)_3{\cdot}9H_2O\\&+ 4.4\,C_2H_5NO_2 \rightarrow Cu_{0.75}Fe_{2.25}O_4 + 8.8\,CO_2\\&+ 33.5\,H_2O + 6.32\,N_2 + 0.45\,O_2\end{aligned} \tag{1}$$

$$\begin{aligned}&1.0\,Cu(NO_3)_2{\cdot}3H_2O + 2.0\,Fe(NO_3)_3{\cdot}9H_2O\\&+ 4.4\,C_2H_5NO_2 \rightarrow CuFe_2O_4 + 8.8\,CO_2\\&+ 32.11\,H_2O + 6.22\,N_2\end{aligned} \tag{2}$$

$$\begin{aligned}&1.25\,Cu(NO_3)_2{\cdot}3H_2O + 1.75\,Fe(NO_3)_3{\cdot}9H_2O\\&+ 4.4\,C_2H_5NO_2 + 0.25\,O_2 \rightarrow Cu_{1.25}Fe_{1.75}O_4 + 8.8\,CO_2\\&+ 30.5\,H_2O + 6.07\,N_2\end{aligned} \tag{3}$$

Here, the stoichiometric mixture (Eq. (2)) does not require atmospheric oxygen to oxidize the fuel completely.

In order to investigate the effect of ambient air on the structural properties of nanoparticles, both open and closed synthesis systems were utilized. The structural properties of $Cu_xFe_{3-x}O_4$ samples obtained in the presence and absence of the air (S1, S2, S3, S4, S5, and S6) were studied by X-ray diffraction (XRD) using PANalytical, X'Pert Pro equipped with crystal monochromator employing Cu-Kα radiation with the wavelength of 0.154056 nm and the patterns were obtained in the 2θ range of 20–80° as shown in Fig. 2. All samples exhibit sharp and well-defined peak profiles. In order to obtain copper ferrite without any impurities, nanoparticle synthesis was carried out in different stoichiometric ratios and in different environments (both in the presence and absence of air). The XRD patterns of the obtained nanoparticles indicate that the compound possesses a cubic spinel structure belonging to the *Fd-3m* space group ($a = b = c$). In this structure, Cu^{2+} ions occupy the tetrahedral sites and Fe^{3+} ions occupy the octahedral sites of the crystal lattice [26]. The graph shows all the characteristic peaks of copper ferrite and is well-matched with the standard ICDD no. 98-003-7429. Along with this, there are α-Fe_2O_3 peaks corresponding to the ICDD card no. 98-016-1291 for S1, S3, S4, S5, and S6. The formation of α-Fe_2O_3 peaks is caused by the oxidation of Fe^{2+} to Fe^{3+} due to the reaction of iron nitrate with glycine in the presence of air (Eq. (4)). This is attributed to the participation of atmospheric oxygen in the combustion reaction [27]. S3 and S4 samples showed monoclinic CuO peaks which were consistent with the reference data listed on the ICDD no. 00-045-0937. It is attributed to the low efficiency in the concentration of the precursor used as the primary source of -OH groups in the reaction, regardless of the stoichiometric ratio. The absence of -OH groups in the reaction can cause the formation of oxide compounds (α-Fe_2O_3 and CuO) of Fe^{3+} and Cu^{2+} ions due to high-temperature heating processes [28].

$$4\,Fe_3O_4 + O_2 \rightarrow 6\,Fe_2O_3 \quad (4)$$

The results obtained from the XRD analysis clearly demonstrate that the formation of α-Fe_2O_3 within the structure of the synthesized nanoparticles was significantly higher in the open system due to the influence of oxygen in the air, compared to the closed system.

The average crystallite size of the nanoparticles was calculated using the Scherrer formula given in Eq. (5):

$$D = \frac{k\lambda}{\beta \cos\theta} \quad (5)$$

where, D is the average crystallite size (nm), k is a constant equal to 0.9, λ is the wavelength of radiation, β is the full width at half maximum (rad) and θ is the Bragg's diffraction angle (rad). The average crystallite sizes were found to be 41.23, 43.27, 39.89, 55.65, 41.25, and 54.46 nm for S1, S2, S3, S4, S5, and S6, respectively. Equation (6), given below, was used to calculate the lattice parameters of nanoparticles.

$$\frac{1}{d_{hkl}^2} = \frac{(h^2 + k^2 + l^2)}{\alpha^2} \quad (6)$$

where, d is the distance between the crystal planes, h, k, and l are the miller indices and a is the lattice parameter. The values of lattice parameters with the distance between the crystal planes are presented in Table 2.

Table 2 XRD parameters of $Cu_xFe_{3-x}O_4$ nanoparticles

Sample	d_{311} (Å)	α (Å)	Crystallite size (nm)
S1	2.53159	8.3963	41.23
S2	2.54851	8.4524	43.27
S3	2.52587	8.3773	39.89
S4	2.52942	8.3691	55.65
S5	2.53162	8.3964	41.25
S6	2.52545	8.3759	54.46

3.2 FTIR analysis

FTIR analysis of the $Cu_xFe_{3-x}O_4$ nanoparticles was performed in the 400–4000 cm^{-1} frequency range to attain more information about the formation and chemical bond of spinel ferrites as shown in Fig. 3. The vibrations attributed to the absorption of $CuFe_2O_4$ metal oxide at tetrahedral and octahedral sites, which are observed within the frequency range of 400–1000 cm^{-1}, are a result of the Fe–O and Cu–O occupancy sites [19]. The bands centered at ~594 and ~670 cm^{-1} are attributed to the octahedral site and result from the stretching vibration of the $Cu^{2+}-O^{2-}$ bond [28, 29]. The bands located at ~474 and ~547 cm^{-1} correspond to the tetrahedral site, which is attributed to the $Fe^{3+}-O^{2-}$ stretching vibration [30, 31]. The presence of these characteristics in the FTIR spectra of the ferrites confirms the formation of bonds in the sub-lattices of the spinel structure. The absorption bands observed around 2080 cm^{-1} indicate the presence of stretching vibrations corresponding to the C≡N bonds, which can be attributed to the nitrate ligands present in the precursor material [32, 33]. It was observed that the bands corresponding to the 474 cm^{-1} for S3, S4, S5, and S6 have shifted to higher frequencies (Fig. 3b). It can be explained by the displacement of Fe^{3+} ions from the octahedral site to the tetrahedral site [34].

3.3 Thermal analysis

In order to understand the thermal behavior of the precursors, the gelatinous masses obtained from different ratios were heated from 20 to 1200 °C with a heating rate of 20 °C/min by using thermal gravimetric analysis (TGA) and differential scanning calorimetry (DSC). For the same ratios, only one analysis is sufficient (no separate analyses were performed for open and closed systems), so S1 and S2, S3 and S4, and S5 and S6 are shown together in Fig. 4. From the TGA curves, it is observed that there are three temperature stages indicating weight loss. The first stage corresponding to 50–140 °C exhibits a narrow and distinct endothermic peak with a weight loss of ~%3, which can be attributed to the evaporation of remaining water as well as the desorption of absorbed water from the gelatinous mass [35]. In the second stage (140–200 °C), exothermic peaks are observed at 144, 147, and 159 °C for S1-S2, S3-S4, and S5-S6, respectively. These peaks are attributed to the

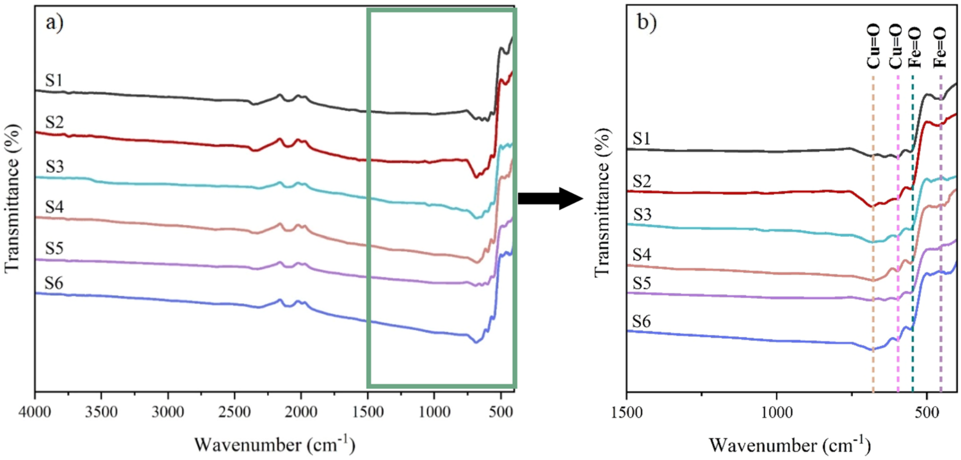

Fig. 3 FTIR spectrum of $Cu_xFe_{3-x}O_4$ nanoparticles

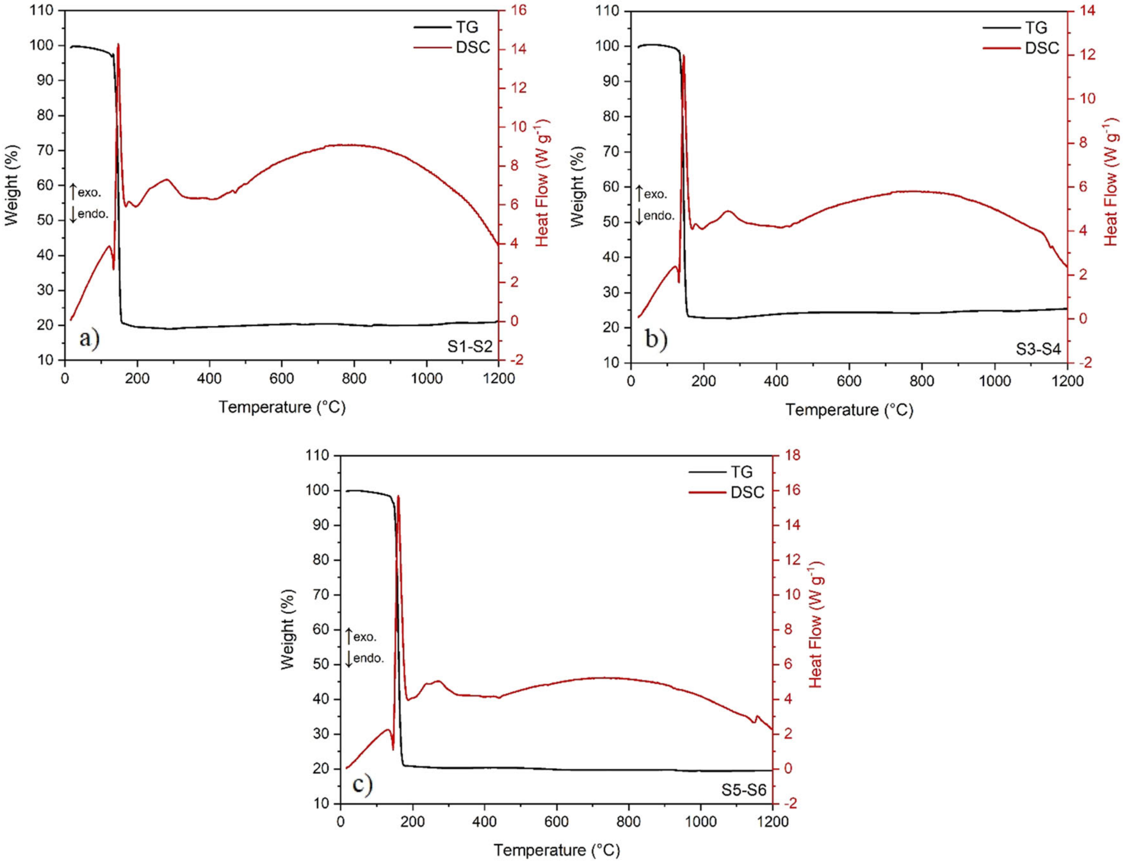

Fig. 4 TGA–DSC curves of solution precursors: **a** S1-S2, **b** S3-S4, **c** S5-S6

combustion reactions between nitrates and glycine, resulting in a significant weight loss of about % 77 in the TGA curves. The weight loss remains constant in the third stage (above 200 °C) [36]. The small peaks around 280 °C may be assigned to the slow oxidation of organic residues [27]. In addition, in Fig. 4b, c an endothermic peak at 1152 °C can be attributed to the decomposition of the spinel structure into CuO and α-Fe_2O_3 [37, 38].

3.4 Morphological analysis

Figure 5 shows the porous structure of the solution-combusted nanoparticles synthesized at different conditions. It was observed that the nanoparticles agglomerated due to their magnetic properties, resulting in a mass of various agglomerations with a wide distribution. On the other hand, it is also observed that as a result of the gases

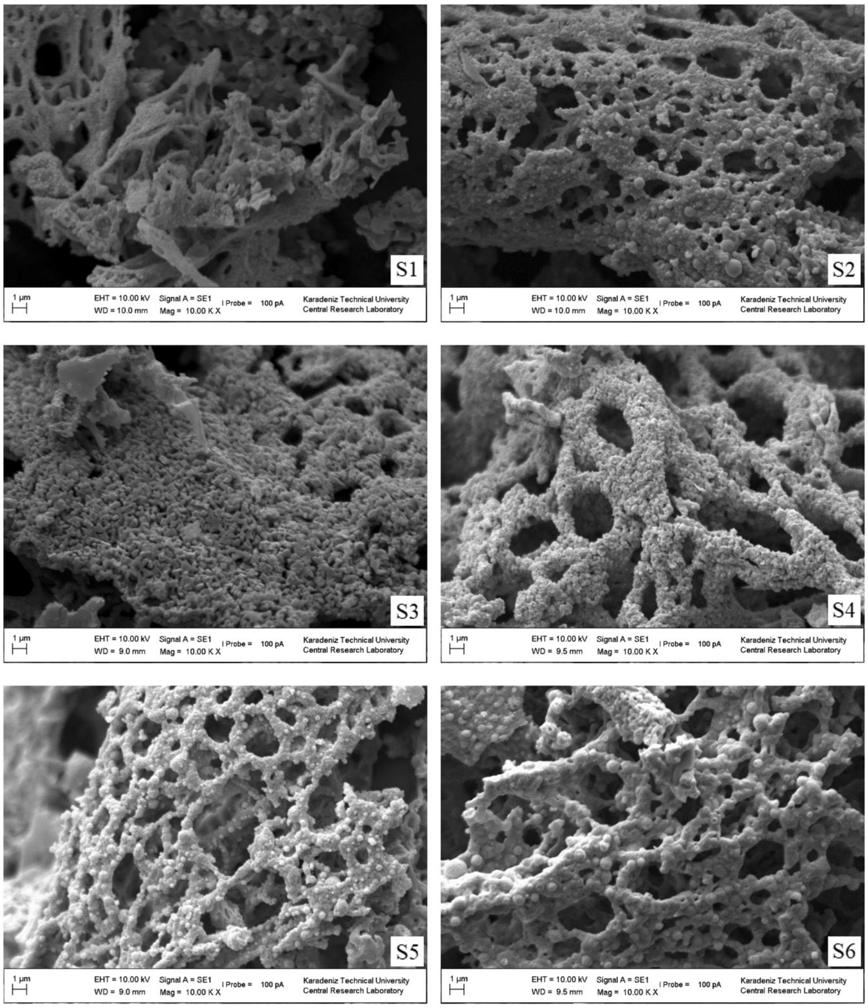

Fig. 5 SEM images of the solution combusted nanoparticles at presence of air (S1, S3, S5) and absence of air (S2, S4, S6)

released during the combustion process, the agglomerated particles exhibit irregularly sized and shaped voids and a porous network structure. The differences between the nanostructures are the results of carrying out the combustion reaction in different environments.

The unique morphologies of SCS products suggest that the particles have a tendency to aggregate due to the influence of nanoscale effects. However, the gases released during the combustion process have a dispersant effect on these agglomerates, leading to the formation of irregularly sized and shaped voids and a porous network structure. Furthermore, the high energy generated during the combustion reaction process can accelerate the crystal growth of these particles, leading to the formation of a highly porous and interconnected structure. Overall, these complex phenomena contribute to the distinctive morphologies and properties of SCS products [39, 40].

The TEM and HRTEM images of stoichiometric copper ferrite nanoparticles are shown in Fig. 6. It can be clearly seen in TEM images (Fig. 6a, b) that nanoparticles are agglomerated and not visible individually. Moreover, this observation is further supported by SEM images. However, upon careful examination of the TEM images, it is observed that nanoparticle clusters are agglomerated in a porous manner, with sizes ranging between 15–55 nm and an average particle size of 35.6 nm (Fig. 6d). The HRTEM image of nanoparticles (Fig. 6c) confirmed the presence of clear lattice fringes with a distinct *d* value of 0.25 nm, corresponding to the (311) plane, which agrees with the (311) plane in the XRD results presented in Table 2.

3.5 Magnetic properties

The magnetic properties of the solution-combusted $Cu_xFe_{3-x}O_4$ nanoparticles were investigated using a vibrating sample magnetometer (VSM) at room temperature and the magnetization loops are shown in Fig. 7. Magnetic properties depend on cation distribution, crystallinity, crystallite size, phase composition, and particle size [41]. The saturation magnetization (M_s), remnant magnetization (M_r), and coercivity (H_c) values are also presented in Table 3. According to the magnetic hysteresis curves saturation magnetization values were found to be 47.36,

Fig. 6 **a**, **b** TEM images of stoichiometric $Cu_xFe_{3-x}O_4$ (S2) nanoparticles, **c** Lattice-resolved HRTEM image of S2 nanoparticles, **d** Particle size distribution of S2 nanoparticles

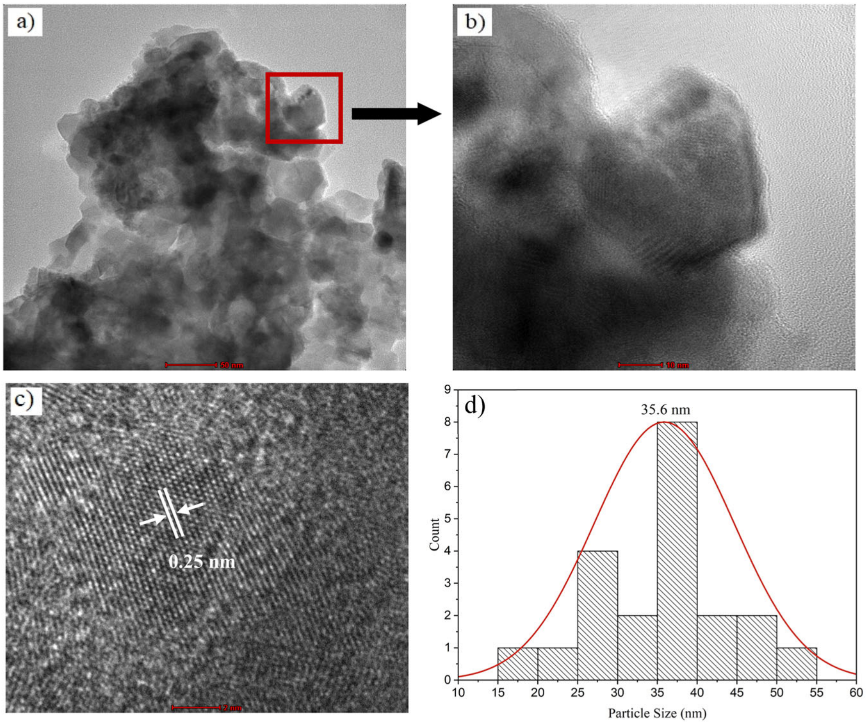

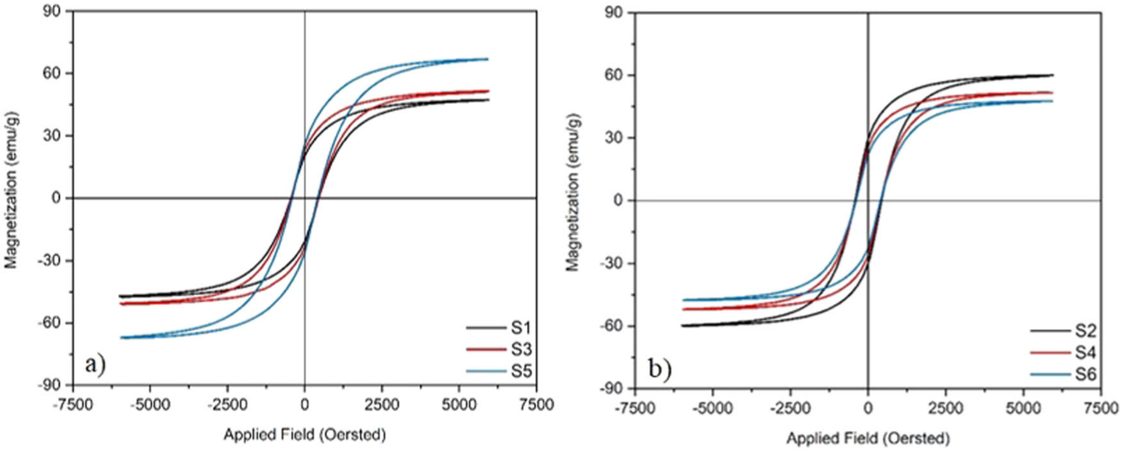

Fig. 7 Magnetization loops of (**a**) S1, S3, S5 and (**b**) S2, S4, S6 nanoparticles prepared by solution combustion synthesis

51.59, and 66.92 emu/g for S1, S3, and S5, respectively. For S2, S4, and S6 the saturation magnetization values are obtained as 60.15, 51.59, and 47.62 emu/g, respectively. The results revealed that for the open systems S5 shows the highest M_s value than S3 and S1. This is attributed to the amount of α-Fe_2O_3 impurities in the structure. Figure 2b shows the comparison of peak intensities and peak positions for S1, S3, and S5. XRD results clearly show that the samples contain secondary non-magnetic Fe_2O_3 phases. It is possible that the formation of α-Fe_2O_3 could be a result of the decomposition of ferrite [42, 43]. Another reason for the presence of α-Fe_2O_3 in the structure is the reaction of Fe_3O_4

Table 3 The different magnetic parameters obtained from magnetic hysteresis curves of $Cu_xFe_{3-x}O_4$ nanoparticles

Sample	Saturation magnetization (M_s, emu/g)	Remnant magnetization (M_r, emu/g)	Coercivity (H_c, Oe)
S1	47.36	20.27	448.01
S2	60.15	29.49	427.49
S3	51.59	23.17	444.59
S4	51.69	25.51	406.97
S5	66.92	25.92	410.39
S6	47.62	22.41	396.71

Table 4 Magnetic properties of $CuFe_2O_4$ nanoparticles reported in literature

Synthesis technique	Saturation magnetization (M_s, emu/g)	Coercivity (H_c, Oe)	References
Solution combustion	60.15	427.49	Present work
Sol-gel	42.23	35.98	[45]
Electrospinning	23.98	625	[46]
Hydrothermal	33.67	28.3	[47]
Hydrothermal	22.12	13.67	[48]
Solution combustion	18.1	177	[49]

with oxygen, as shown in Eq. (6). Therefore, it is observed that the magnetic property is poor in samples including higher levels of α-Fe_2O_3 impurities. Figure 2c shows the peak intensities for S2, S4, and S6. Due to similar reasons, S2 shows a higher value compared to S4 and S6 with a M_s value of 60.15 emu/g. The copper ferrite is an inverse spinel. The alignment of Cu^{2+} ions in the tetragonally distorted octahedral spinel lattice formed by oxygen ions can be triggered by copper ions in substituted spinels via a collective Jahn–Teller effect. The migration of Cu^{2+} cations from the octahedral sites of the B-sublattice to the tetrahedral sites of the A-sublattice is considered to have a significant effect on the magnetic properties of $CuFe_2O_4$ [44]. Table 4 presents the values of M_s and H_c for $CuFe_2O_4$ nanoparticles synthesized using different methods in the literature. The table shows that the values obtained in this study are in line with those reported in previous works.

4 Conclusions

In the present research, the effect of atmosphere on the structure, FTIR, thermal properties, morphology, and magnetic properties of $Cu_xFe_{3-x}O_4$ nanoparticles have been studied and presented. From the XRD analysis, the spinel structures of ferrites were verified and the effect of air on the formation of secondary phases was observed. The presence of Fe–O and Cu–O bonds observed in the FTIR analysis indicates that the obtained nanoparticles are spinel copper ferrites. The formation of exothermic and endothermic peaks in the DSC-TGA analyses proves that combustion reaction has occurred. The SEM images reveal that the nanoparticles agglomerate due to their magnetic properties, but there are voids between the agglomerated particles resulting from the gas formation. The TEM and HRTEM results show that the nanoparticles are agglomerated in a porous manner with an average particle size of 35.6 nm. The HRTEM image confirms the presence of clear lattice fringes corresponding to the (311) plane. The VSM results indicate that the material exhibits magnetic properties, however, the formation of the Fe_2O_3 phase, as a secondary phase, reduces the saturation magnetization of the nanoparticles. The significance of the absence of air during the synthesis process was clearly observed through the analyses conducted on the synthesized products.

Compliance with ethical standards

Conflict of interest The authors declare no competing interests.

References

1. Lazarova T, Georgieva M, Tzankov D, Voykova D, Aleksandrov L, Cherkezova-Zheleva Z, Kovacheva D (2017) Influence of the type of fuel used for the solution combustion synthesis on the structure, morphology and magnetic properties of nanosized $NiFe_2O_4$. J Alloy Compd 700:272–283
2. Houshiar M, Zebhi F, Razi ZJ, Alidoust A, Askari Z (2014) Synthesis of cobalt ferrite ($CoFe_2O_4$) nanoparticles using combustion, coprecipitation, and precipitation methods: A comparison study of size, structural, and magnetic properties. J Magn Magn Mater 371:43–48
3. Vinosha PA, Mely LA, Jeronsia JE, Krishnan S, Das SJ (2017) Synthesis and properties of spinel $ZnFe_2O_4$ nanoparticles by facile co-precipitation route. Optik 134:99–108
4. Selvan RK, Augustin CO, Berchmans LJ, Saraswathi R (2003) Combustion synthesis of $CuFe_2O_4$. Mater Res Bull 38:41–54
5. Aslibeiki B, Kameli P, Ehsani MH, Salamati H, Muscas G, Agostinelli E, Foglietti V, Casciardi S, Peddis D (2016) Solvothermal synthesis of $MnFe_2O_4$ nanoparticles: the role of polymer coating on morphology and magnetic properties. J Magn Magn Mater 399:236–244
6. Liu YC, Fu YP (2010) Magnetic and catalytic properties of copper ferrite nanopowders prepared by a microwave-induced combustion process. Ceram Int 36(5):1597–1601
7. Gingasu D, Mindru I, Patron L, Cizmas C-B (2008) Tetragonal copper ferrite obtained by self-propagating combustion. J Alloy Compd 460(1-2):627–631
8. Estrella M, Barrio L, Zhou G, Wang X, Wang Q, Wen W, Hanson JC, Frenkel AI, Rodriguez JA (2009) In situ characterization of $CuFe_2O_4$ and Cu/Fe_3O_4 water-gas shift catalysts. J Phys Chem C 113:14411–14417
9. Manova E, Tsoncheva T, Paneva D, Popova M, Velinov N, Kunev B, Tenchev K, Mitov I (2011) Nanosized copper ferrite materials: mechanochemical synthesis and characterization. J Solid State Chem 184(5):1153–1158
10. Zhuravlev VA, Minin RV, Itin VI, Lilenko IY (2017) Structural parameters and magnetic properties of copper ferrite nanopowders obtained by the sol-gel combustion. J Alloy Compd 692:705–712
11. Sun Z, Liu L, Jia DZ, Pan W (2007) Simple synthesis of $CuFe_2O_4$ nanoparticles as gas-sensing materials. Sens Actuators B 125(1):144–148
12. Xing Z, Ju Z, Yang J, Xu H, Qian Y (2013) One-step solid state reaction to selectively fabricate cubic and tetragonal $CuFe_2O_4$ anode material for high power lithium ion batteries. Electrochim Acta 102:51–57
13. Rani BJ, Saravanakumar B, Ravi G, Ganesh V, Ravichandran S, Yuvakkumar R (2017) Structural, optical and magnetic properties of $CuFe_2O_4$ nanoparticles. J Mater Sci Mater Electron 29(3):1975–1984

14. Li XH, Xu CL, Han XH, Qiao L, Wang T, Li FS (2010) Synthesis and magnetic properties of nearly monodisperse $CoFe_2O_4$ nanoparticles through a simple hydrothermal condition. Nanoscale Res Lett 5(6):1039–1044
15. Huang Z, Zhu Y, Zhang J, Yin G (2007) Stable biomimetic superhydrophobicity and magnetization film with Cu-Ferrite nanorods. J Phys Chem C 111:6821–6825
16. Zhu M, Meng D, Wang C, Diao G (2013) Facile fabrication of hierarchically porous $CuFe_2O_4$ nanospheres with enhanced capacitance property. Appl Mater Interfaces 5(13):6030–6037
17. Karthigayan N, Manimuthu P, Priya M, Sagadevan S (2017) Synthesis and characterization of $NiFe_2O_4$, $CoFe_2O_4$ and $CuFe_2O_4$ Thin films for anode material in li-ion batteries. Nanomater Nanotechnol 7:1–5
18. Malana MA, Qureshi RB, Ashiq MN, Zafar ZI (2013) Synthesis, electrical and dielectric characterization of cerium doped nano copper ferrites. Mater Res Bull 48(11):4775–4779
19. Kombaiah K, Vijaya JJ, Kennedy LJ, Bououdina M, Al-Najar B (2018) Conventional and microwave combustion synthesis of optomagnetic $CuFe_2O_4$ nanoparticles for hyperthermia studies. J Phys Chem Solids 115:162–171
20. Kombaiah K, Vijaya JJ, Kennedy LJ, Bououdina M, Ramalingam RJ, Al-Lohedan HA (2017) Comparative investigation on the structural, morphological, optical, and magnetic properties of $CoFe_2O_4$ nanoparticles. Ceram Int 43(10):7682–7689
21. Pourgolmohammad B, Masoudpanah SM, Aboutalebi MR (2017) Effect of starting solution acidity on the characteristics of $CoFe_2O_4$ powders prepared by solution combustion synthesis. J Magn Magn Mater 424:352–358
22. Alves AK, Bergmann CP, Berutti FA (2013) Novel synthesis and characterization of nanostructured materials. Springer Science +Business Media, Berlin
23. Raja G, Saranya R, Saravanan K (2018) Microwave combustion method: effect of starch, urea and glycine as processing fuels in the Co_3O_4 nanostructures. Optik 153:73–80
24. Umadevi M, Christy AJ (2013) Synthesis, characterization and photocatalytic activity of CuO nanoflowers. Spectrochim Acta A 109:133–137
25. Sudheesh VD, Thomas N, Roona N, Baghya PK, Sebastian V (2017) Synthesis, characterization and influence of fuel to oxidizer ratio on the properties of spinel ferrite (MFe_2O_4, M = Co and Ni) prepared by solution combustion method. Ceram Int 43(17):15002–15009
26. Cui K, Sun M, Gong T, Xu J, Hou L, Yuan C (2022) Construction of single-crystal nanoparticles assembled $CuFe_2O_4$ spinel microspheres towards high infrared emissivity. J Alloys Compd 929:167365
27. Ianoş R, Tăculescu A, Păcurariu C, Lazău I, Joy P (2012) Solution combustion synthesis and characterization of magnetite, Fe_3O_4, nanopowders. J Am Ceram Soc 95(7):2236–2240
28. Cahyana AH, Liandi AR, Yulizar Y, Romdoni Y, Wendari TP (2021) Green synthesis of $CuFe_2O_4$ nanoparticles mediated by Morus alba L. leaf extract: crystal structure, grain morphology, particle size, magnetic and catalytic properties in Mannich reaction. Ceram Int 47(15):21373–21380
29. Dippong T, Deac IG, Cadar O, Levei EA, Petean I (2020) Impact of Cu^{2+} substitution by Co^{2+} on the structural and magnetic properties of $CuFe_2O_4$ synthesized by sol-gel route. Mater Charac 163:110248
30. İçin K, Öztürk S, Çakıl DD, Sünbül SE (2021) Mechanochemical synthesis of $SrFe_{12}O_{19}$ from recycled mill scale: Effect of synthesis time on phase formation and magnetic properties. J Alloys Compd 873:159787
31. Fathi H, Masoudpanah SM, Alamolhoda S, Parnianfar H (2017) Effect of fuel type on the microstructure and magnetic properties of solution combusted fe3o4 powders. Ceram Int 43(10):7448–7453
32. Moosvi SK, Majid K, Ara T (2016) Studying the electrical, thermal, and photocatalytic activity of nanocomposite of polypyrrole with the photoadduct of $K_3[Fe(CN)_6]$ and Diethylenetriamine. Mater Res 19(5):983–990
33. Horch M, Lauterbach L, Saggu M, Hildebrandt P, Lendzian F, Bittl R, Lenz O, Zebger I (2010) Probing the active site of an O_2−tolerant NAD^+−reducing [NiFe]-hydrogenase from Ralstonia eutropha H16 by in situ EPR and FTIR spectroscopy. Angew Chem Int Ed 49(43):8026–8029
34. Rathod SM, Chavan AR, Jadhav SS, Batoo KM, Hadi M, Raslan EH (2021) Ag^+ ion substituted $CuFe_2O_4$ nanoparticles: analysis of structural and magnetic behavior. Chem Phys Lett 765:138308
35. Mazrouei A, Saidi A (2018) Microstructure and magnetic properties of cobalt ferrite nano powder prepared by solution combustion synthesis. Mater Chem Phys 209:152–158
36. Wang X, Qin M, Fang F, Jia B, Wu H, Qu X, Volinsky AA (2017) Effect of glycine on one-step solution combustion synthesis of magnetite nanoparticles. J Alloy Compd 719:288–295
37. Shanmugavani A, Selvan RK (2016) Improved electrochemical performances of $CuCo_2O_4$/CuO nanocomposites for asymmetric supercapacitors. Electrochim Acta 188:852–862
38. Li NH, Lo SL, Hu CY, Hsieh CH, Chen CL (2011) Stabilization and phase transformation of $CuFe_2O_4$ sintered from simulated copper-laden sludge. J Hazard Mater 190(1-3):597–603
39. Rodríguez MA, Aguilar CL, Aghayan MA (2012) Solution combustion synthesis and sintering behavior of $CaAl_2O_4$. Ceram Int 38(1):395–399
40. Toniolo J, Takimi AS, Andrade MJ, Bonadiman R, Bergmann CP (2007) Synthesis by the solution combustion process and magnetic properties of iron oxide (Fe_3O_4 and α-Fe_2O_3) particles. J Mater Sci 42(13):4785–4791
41. Aali H, Mollazadeh S, Khaki JV (2018) Single-phase magnetite with high saturation magnetization synthesized via modified solution combustion synthesis procedure. Ceram Int 44(16):20267–20274
42. Ranjith Kumar E, Jayaprakash R, Chandrasekaran J (2013) Effect of fuel ratio and the impact of annealing temperature on particle size, magnetic and dielectric properties of manganese substituted $CuFe_2O_4$ nanoparticles. Superlattices Microstruct 64:343–353
43. Laokul P, Amornkitbamrung V, Seraphin S, Maensiri S (2011) Characterization and magnetic properties of nanocrystalline $CuFe_2O_4$, $NiFe_2O_4$, $ZnFe_2O_4$ powders prepared by the aloe vera extract solution. Curr Appl Phys 11(1):101–108
44. Nedkov I, Vandenberghe RE, Marinova T, Thailhades P, Merodiiska T, Avramova I (2006) Magnetic structure and collective Jahn–Teller distortions in nanostructured particles of $CuFe_2O_4$. Appl Surf Sci 253(5):2589–2596
45. Raja G, Gopinath S, Raj RA, Shukla AK, Alhoshan MS, Sivakumar K (2016) Comparative investigation of $CuFe_2O_4$ nano and microstructures for structural, morphological, optical and magnetic properties. Phys E Low Dimens 83:69–73
46. Ponhan W, Maensiri S (2009) Fabrication and magnetic properties of electrospun copper ferrite ($CuFe_2O_4$) nanofibers. Solid State Sci 11(2):479–484
47. Kurian J, Jacob MM (2017) A facile approach to the elucidation of magnetic parameters of $CuFe_2O_4$ nanoparticles synthesized by hydrothermal route. J Magn Magn Mater 428:204–212
48. Paramasivan P, Venkatesh P (2016) Controllable synthesis of $CuFe_2O_4$ nanostructures through simple hydrothermal method in the presence of thioglycolic acid. Phys E Low Dimens 84:258–262
49. Vergis BR, Hari Krishna R, Kottam N, Nagabhushana BM, Sharath R, Darukaprasad B (2017) Removal of malachite green from aqueous solution by magnetic $CuFe_2O_4$ nano-adsorbent synthesized by one pot solution combustion method. J Nanostructure Chem 8(1):1–12